Water SA 51(3) 268–278 / Jul 2025
https://doi.org/10.17159/wsa/2025.v51.i3.4156

Subsidence and evaporation in South African dry spells

Mark R Jury[1,2]

[1]*Geography Dept, University of Zululand, KwaDlangezwa, South Africa*
[2]*Physics Dept, University of Puerto Rico, Mayagüez, Puerto Rico, USA*

The intensity of dry spells in South Africa is evaluated with monthly European Reanalysis potential evaporation which describes the rate of soil moisture depletion. Filtered time series of potential evaporation averaged over eastern South Africa for 1960–2022 provide a basis for meteorological analysis. After ranking, a representative dry summer (Oct 2018 – Feb 2019) and case study (10–14 Dec 2018), emerged. The synoptic circulation was dominated by upper level equatorward airflow and mid-level subsidence of –0.1 m/s. Back-trajectory analysis shows how warm, dry, dusty air spreads eastward from the Namib Desert to the Orange River Valley, while sinking from 3 000 to 1 000 m. Diurnal evaporation exceeded 0.6 mm/h and dewpoint temperatures of –9°C were recorded in the Free State Province. Global statistics confirm that Pacific El Niño and warm phase Indian Ocean Dipole lead to unusually dry summer weather. Terrestrial runoff and river discharge across eastern South Africa are equally correlated with rainfall and potential evaporation (±0.74), suggesting that operational monitoring and applied research should put greater emphasis on hydrological losses and surface water demand.

CORRESPONDENCE
Mark R Jury

EMAIL
mark.jury@upr.edu

DATES
Received: 17 January 2025
Accepted: 7 June 2025

KEYWORDS
subsidence
Namib airmass outflow
South African drought
potential evaporation

INTRODUCTION

South Africa lies between two anticyclonic ocean–atmosphere gyres over the southwest Indian and southeast Atlantic that instil an east–west humidity gradient across the elevated plateau. Wind-driven upwelling limits humidity over the cool Benguela Current and westerly winds spread the dry airmass across the Kalahari during winter. In contrast, warm sea temperatures promote atmospheric convection over the Agulhas Current. Easterly winds lift the humid air over the Drakensberg escarpment during summer and support agricultural production. The seasonally alternating zonal circulation largely determines whether rainfall prevails over evaporation (Mason and Jury, 1997; Driver and Reason, 2017; Blamey et al., 2018).

In the background, the descending branch of the Hadley circulation entrains into the subtropical anticyclones straddling South Africa. These can merge and block tropical outflows from the Zambezi or separate and allow NW cloud-bands to extend poleward. Global coupled teleconnections can shift the cloud-band axis from South Africa to Madagascar during anomalous sea surface temperature (SST) and jet stream activity associated with positive phase Indian Ocean Dipole (IOD) and Pacific El Niño Southern Oscillation (ENSO) (Lindesay and Vogel, 1990; Hart et al., 2018). When these two phenomena coincide, a trough over the Mozambique Channel induces subsiding equatorward airflow over South Africa (Malherbe et al., 2016; Chikoore and Jury, 2021).

Dry spells are characterized by sunny skies and hot, windy weather that deplete soil moisture via potential evaporation (Lyon, 2009). The rate of desiccation may be quantified by: (i) hourly weather data, (ii) model heat flux, or (iii) daily evaporation pan. Such measures have spatial homogeneity, temporal persistence, wide representivity, and offer steady information that is relatively independent of station density or advances in models and satellites (unlike rainfall).

Here surface potential evaporation from the European Reanalysis (ERA5, Hersbach et al., 2020) is used to quantify the frequency and intensity of dry spells over the agriculturally productive eastern half of South Africa. The research compares this product with sensible heat flux (SHF) and pan measurements, and analyses the geographical sources of dry air and associated meteorology. Data and methods are followed by results divided into subsections on dry climate, intra-seasonal fluctuations, and inter-annual forcing. A representative dry spell in Dec 2018 is used to elucidate weather-scale processes. A summarizing discussion highlights key points emerging from the research and actionable recommendations. Of particular concern is that studies on the surface water balance often mistakenly utilize precipitation minus actual evaporation, instead of potential evaporation.

DATA AND METHODS

Desiccation across eastern South Africa (eSA, Fig. 1a) 24–33°S, 24–32°E is characterized by ERA5 monthly potential evaporation (pot.evap) in the period 1960–2022. It is derived from SHF via model-estimated surface thermal turbulence (Mauder et al., 2007; McMahon et al., 2013; Maes et al., 2018). ERA5 pot.evap is compared with Climate Research Unit (CRU4) pot.evap (Harris et al., 2020) based on weather station inputs to the Penman-Monteith (P-M) formula, and from *in situ* S-pan pot.evap measurements near 30°S, 26°E obtained from the South African Hydrology Service (SAHS, 2023). The P-M equation requires net solar radiation, air temperature, air pressure, water vapour deficit, wind speed and empirical constants (Sperna-Weiland et al., 2012). Coupled forecast system v2 (CFS2) reanalysis (Saha et al., 2014) provides hourly pot.evap via SHF, to quantify diurnal variations.

Water resources were analysed via gridded river discharge (Harrigan et al., 2020), surface runoff (Ghigg et al., 2021), and CRU4 interpolated gauge rainfall (Harris et al. 2020). Dataset acronyms are defined in Table 1.

To describe the meteorology of dry spells, ERA5 reanalysis fields were analysed for geopotential height, zonal and meridional winds, vertical motion, and specific humidity. Some of the analyses require satellite measurements since 1980 for: net outgoing longwave radiation (OLR, Lee et al., 2007), river discharge, subsurface ocean conditions (GODAS, Behringer 2007) and vegetation colour fraction (NDVI, Pinzon and Tucker, 2014). A representative dry season is used to develop a methodology for identifying the source regions of dry air.

A time series of potential evaporation was created by averaging monthly ERA5 field data over eSA from 1960–2022. Departures from the mean annual cycle were calculated, a 6-month running mean was applied, and highest values were found by ranking the 63-yr record (Table 2). This revealed the dry season of Oct 2018–Feb 2019 for further study. Given the known link between coastal upwelling in the Benguela Current and atmospheric subsidence over the Namib Desert (Vigaud et al., 2009), the vertical structure of air–sea interactions was analysed. Daily pot.evap measurements identified 11–13 Dec 2018 for meteorological analysis of 500 hPa subsidence, 850 hPa winds and SAWS radiosonde profiles at Bloemfontein (29°S, 26°E). Airflow back-trajectories were computed using the Hysplit method (Stein et al., 2015), and dust aerosol concentrations were mapped from MERRA2 air chemistry data assimilation (Molod et al., 2015). These identified geographical source regions for warm dry air reaching eSA during the case study, 11–13 Dec 2018.

To identify inter-annual oscillations, wavelet spectral analysis was applied to the time series of 6-monthly pot.evap anomalies. Global teleconnections were evaluated by correlating the austral summer (Oct–Mar) pot.evap time series with fields of global Hadley SST (Rayner et al. 2003) and net OLR, southern polar 500 hPa geopotential height, and regional 850 hPa wind anomalies.

Table 1. Dataset acronyms and characteristics

Acronym	Name (variables)	Resolution
CFS2	Coupled Forecast System v2 reanalysis (hourly pot.evap SHF)	30 km
CRU4	Climate Research Unit v4 U.E.A (rainfall, pot.evap P-M)	50 km
EC	European Community GLOFAS (river discharge)	20 km
ERA5	European Reanalysis v5 (pot.evap, geopot.ht, wind, omega, humidity)	30 km
GODAS	Global Ocean Data Assimilation System NOAA (currents, sea temperature)	50 km
GRUN	Global Runoff v2 (terrestrial runoff)	50 km
HADLEY	Hadley Centre v2 (sea temperature)	100 km
MERRA2	NASA air chemistry assimilation (dust concentration)	50 km
NDVI	Normalized Difference Vegetation Index (colour fraction)	10 km
OLR	Satellite net outgoing longwave radiation	100 km
SAHS	South African Hydrological Service (S-pan pot.evap)	Station
SAWS	South African Weather Service (radiosonde profiles)	Station

Table 2. Highest potential evaporation anomalies in the eSA area since 1960 with dewpoint temperature anomalies for comparison. The listing is chronological and represents the centre-point of 6-monthly running means; the case study is bold.

Date	CRU4	ERA5	ERA5
Year month	pot.evap	pot.evap	T dew
1983 1	0.60	0.77	–0.72
1983 2	0.66	0.83	–0.71
1983 3	0.54	0.71	–0.40
1992 1	0.69	0.68	–1.15
1992 2	0.85	0.84	–1.64
1992 3	0.87	0.89	–2.07
1992 4	0.70	0.77	–2.23
2007 2	0.75	0.69	–1.48
2007 3	0.70	0.71	–1.94
2015 10	0.74	0.72	–1.56
2015 11	0.82	0.85	–1.93
2015 12	0.87	0.93	–2.17
2016 1	0.82	0.86	–1.93
2016 2	0.70	0.68	–1.19
2018 10	0.72	0.73	–2.99
2018 11	0.87	0.83	–3.08
2018 12	0.91	0.82	–2.60
2019 1	0.86	0.73	–1.81
2019 8	0.72	0.65	–2.46
2019 9	0.81	0.74	–2.78
2019 10	0.75	0.68	–2.55

For the longer/shorter records with ~ 60/40 degrees of freedom, 95% confidence is reached with $|r| > 0.25$ / 0.30. Lag-correlations for 1960–2022 were calculated between the Oct–Mar eSA pot. evap and the Pacific Nino3.4 SST and Indian Ocean Dipole (IOD) time series (cf. Jury, 2022). Lastly, atmospheric impacts on water resources were analysed by lag-correlation of CRU4 rainfall and ERA5 pot.evap with eSA river discharge and runoff.

RESULTS

Climatic patterns and temporal character

Surface conditions are illustrated for SST and vegetation for the representative dry spell of Oct 18–Feb 19 in Fig. 1a. The cool (16°C) Atlantic / warm (26°C) Indian Ocean pattern is amplified near the coast by the Benguela/Agulhas Currents that convey water equatorward/poleward around the respective anticyclonic gyres. There is a pronounced zonal gradient of vegetation (colour fraction); values decline steadily – 45% (30°E), 30% (27°E), 15% (23°E). The westward decrease is steep across the Eastern Cape (32°S) and fans out in a northward direction.

The filtered eSA-area potential evaporation time series (Fig. 1b) exhibits dry spells of ~5.2 mm/day alternating with wet spells of ~4.1 mm/day, and a weak upward trend +0.006 mm/day per year. CRU4/ERA5 pot.evap fluctuations are coherent (r = +0.88), although derived from weather station P-M / model SHF, respectively. The CRU4 long-term mean of 4.50 mm/day falls slightly below ERA5 at 4.62 mm/day, more so in dry spells. Wavelet spectra (Fig. 1c) exhibit 6–7 yr cycles from 1965–2000 followed by 2- and 4-yr cycles in recent decades. Potential evaporation anomalies > 0.6 σ are listed in Table 2 and highlight the dry spell of Dec 2018 when eSA dewpoint temperatures were ~3°C below normal.

Daily pot.evap data from ERA5 and S-pan measurements at 30°S, 26°E are compared over the dry summer of Jul 2018–Jun 2019 in Fig. 2a. Embedded within the seasonal crest due to sun angle and temperature are synoptic weather pulses that modulate wind and humidity. Reanalysis values are ~2 mm/day below S-pan measurements, which reach 8 mm/day from Oct 18–Feb 19. The SHF map (Fig. 2b) shows the S-pan location on the semi-arid boundary with flux values of ~120 W/m^2. Further west, the zone of negative SHF over the Benguela Current saps heat from the lower atmosphere causing a shallow marine boundary layer. Diurnal cycling of SHF/pot.evap has large amplitude, reaching 0.6 mm/h by midday (Fig. 2c). Sunrise/sunset exhibit sudden jumps, and fluctuations grow in the afternoon when infrequent thunderstorms develop.

Marine conditions

The impact of coastal upwelling in the Benguela Current is analysed by vertical sections in Fig. 3a–c. Equatorward winds > 8 m/s (averaged 33–24°S, Oct 18–Feb 19) drive offshore transport in the upper ocean, causing uplift over the shelf. Sea temperatures are cooled to 16°C, and negative SHF combines with divergent equatorward airflow to sustain atmospheric subsidence of –0.1 m/s. Sinking motions are strongest at ~1 500 m 15°E and create a pool of dry air that spills over the Namib Desert. The marine layer over the Benguela Current is shallow (< 400 m) and humidity outflows are inhibited by anticyclonic winds and the western escarpment. Although such air–sea interactions are well known (Vigaud et al., 2009), here modern high-resolution reanalysis offers a detailed perspective to link coastal upwelling with atmospheric sinking motions that desiccate the interior plateau.

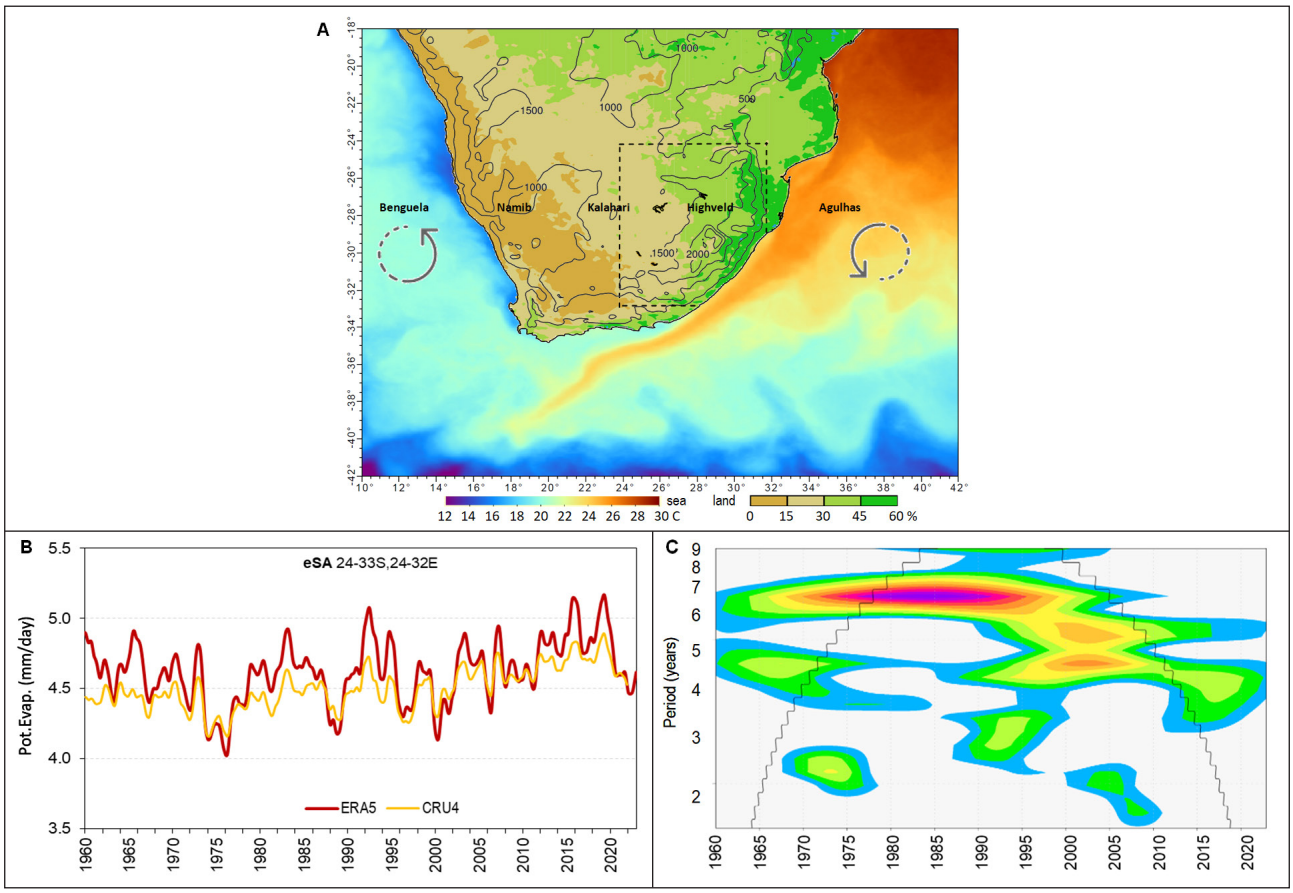

Figure 1. (a) Map of SST and vegetation fraction Oct 2018– eb 2019, topographic contours, dashed eSA area and ocean–atmosphere gyres (schematic rotors), (b) 18-month filtered time series of eSA area CRU4 and ERA5 potential evaporation, and (c) wavelet spectra of ERA5 pot.evap time series shaded 90–99% confidence in log-scale with cone of validity.

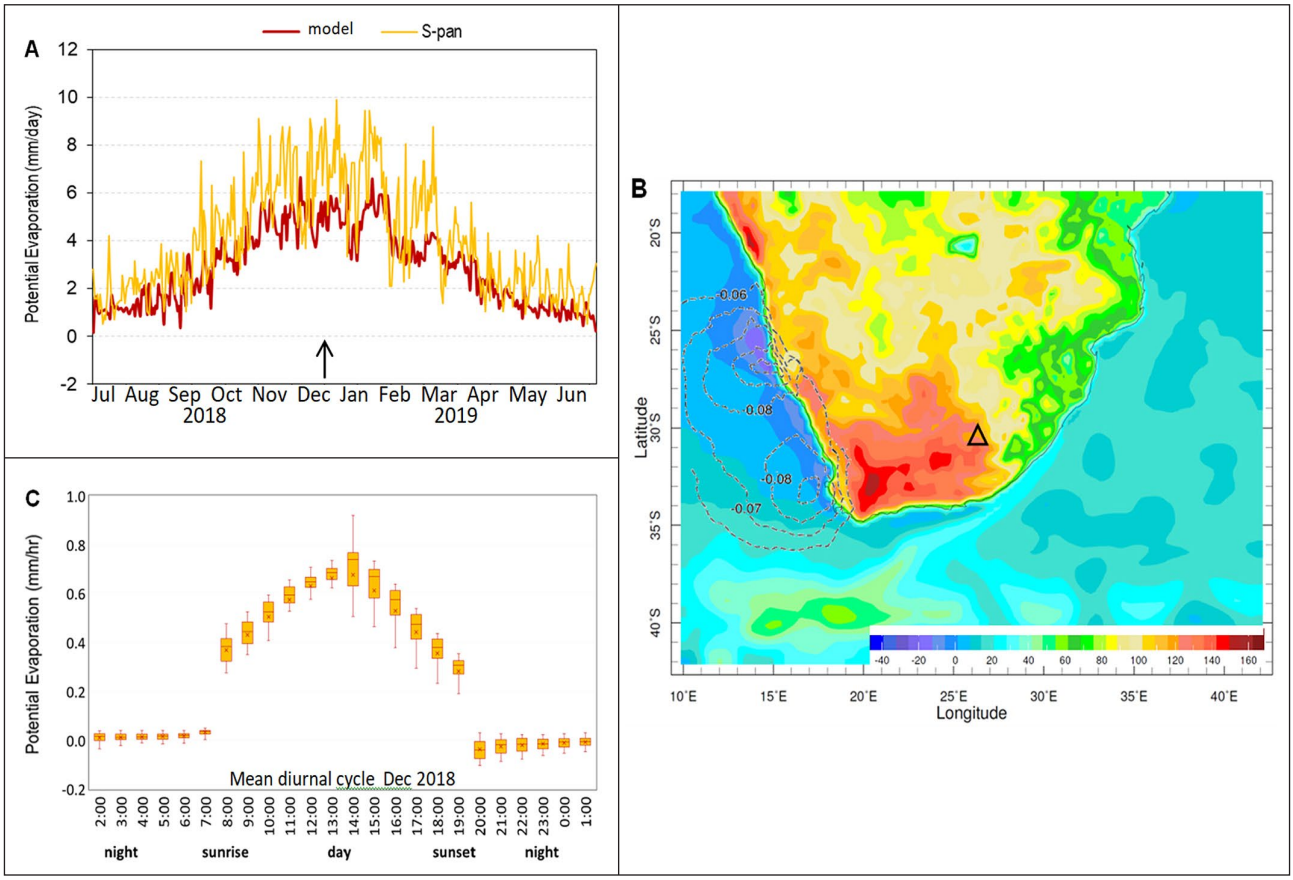

Figure 2. (a) Time series of (unfiltered) daily potential evaporation and S-pan measurement at 30°S, 26°E (Δ on map) with case study arrow, (b) Oct 18–Feb 19 SHF (shaded, W/m^2) and 850–700 hPa subsidence over the Benguela (dashed, m/s), (c) box-whisker plot of mean diurnal cycle for potential evaporation at 30°S, 26°E, based on hourly SHF in Dec 2018 (converted to mm/h)

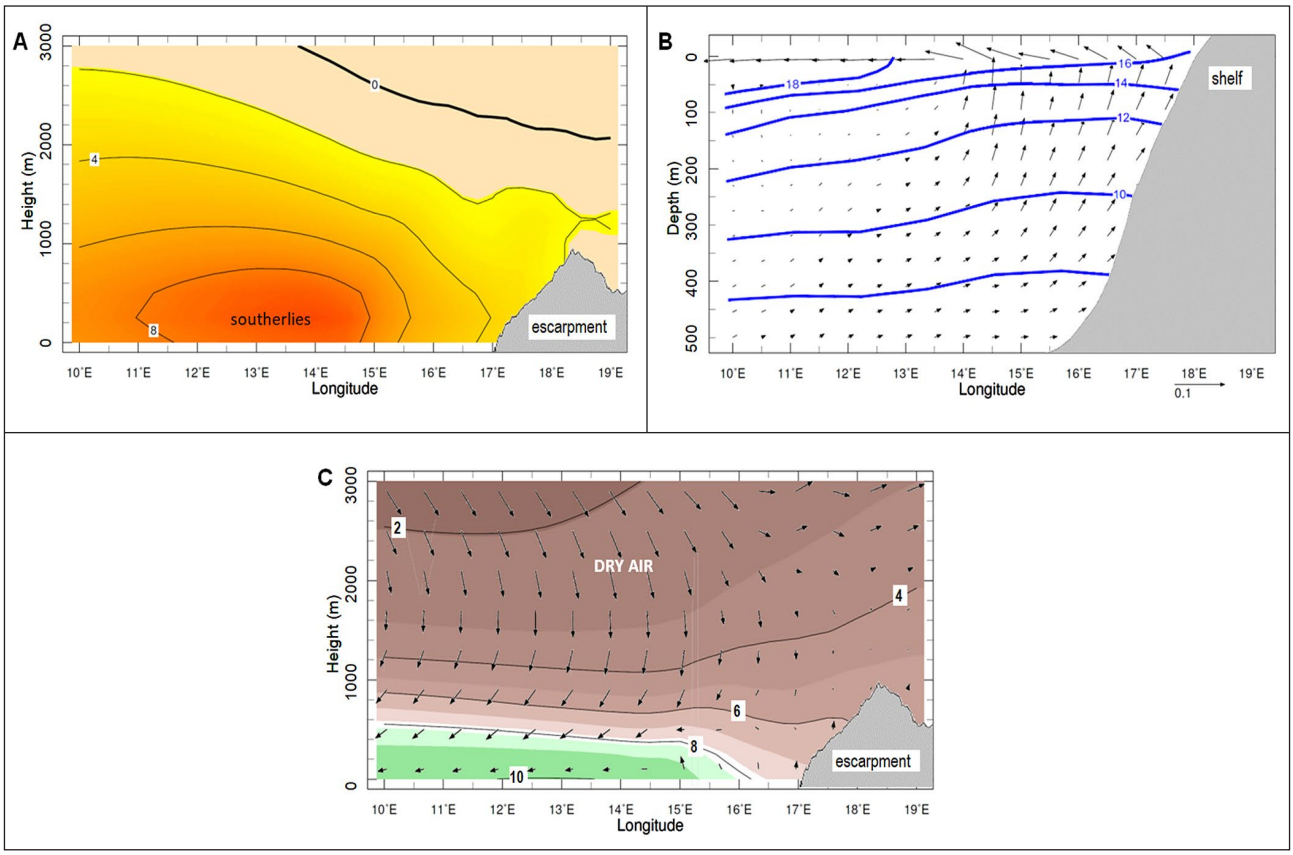

Figure 3. Vertical section plots averaged 24–33°S, Oct 18–Feb 19 in the Benguela–Namib coastal zone: (a) atmospheric low-level V wind, (b) marine upwelling (current vectors, m/s) and sea temperature (isotherms, °C) over the shelf, (c) atmospheric zonal subsiding circulation (largest vector −0.1 m/s) and specific humidity (shaded g/kg) with topographic profile. Values represent totals (not departures).

Oct 18–Feb 19 dry spell and case study

Many dry spells emerging from the potential evaporation time series (Table 2) exhibit common features described earlier by Chikoore and Jury (2022). To provide new insights, the anomalous structure of the Oct 18–Feb 19 season is analysed here. Figure 4a and b illustrate height sections averaged 24–33°S, having sustained upper level equatorward airflow (V~ 5 m/s, 150–300 hPa, 14–22°E) and sinking motion in the layer 300–850 hPa. These are linked conceptually according to Holton (1992): $W = V(\Delta Z)(\beta/f)$ where ΔZ is tropospheric thickness and β describes the cross-latitude fetch of airflow that undergoes a change in Coriolis df/dy. The resulting subsidence warms and dries the atmosphere across the Kalahari.

The case study of Dec 2018 reveals a trough–ridge pattern passing eastward at ~7 m/s (Fig. 4c), bringing mid-tropospheric subsidence of −0.1 m/s. The weather sequence of 10–13 Dec (Fig. 5a–c) shows a zonal overturning circulation with atmospheric subsidence at 600 hPa 18°E on 10 Dec deepening to 450 hPa 28°E on 11 Dec. By 12 Dec 2018 a mid-latitude low pressure cell initiated dry westerly winds over the interior plateau. Maximum and dewpoint temperatures on 13 Dec were 37°C and −9°C, respectively. The radiosonde profile measured upper level equatorward winds of ~20 m/s on 10–11 Dec and excessive dewpoint depressions. Potential evaporation had depleted soil moisture and vegetation to ~15% (cf. Fig. 1a), so there was little moisture available for recycling.

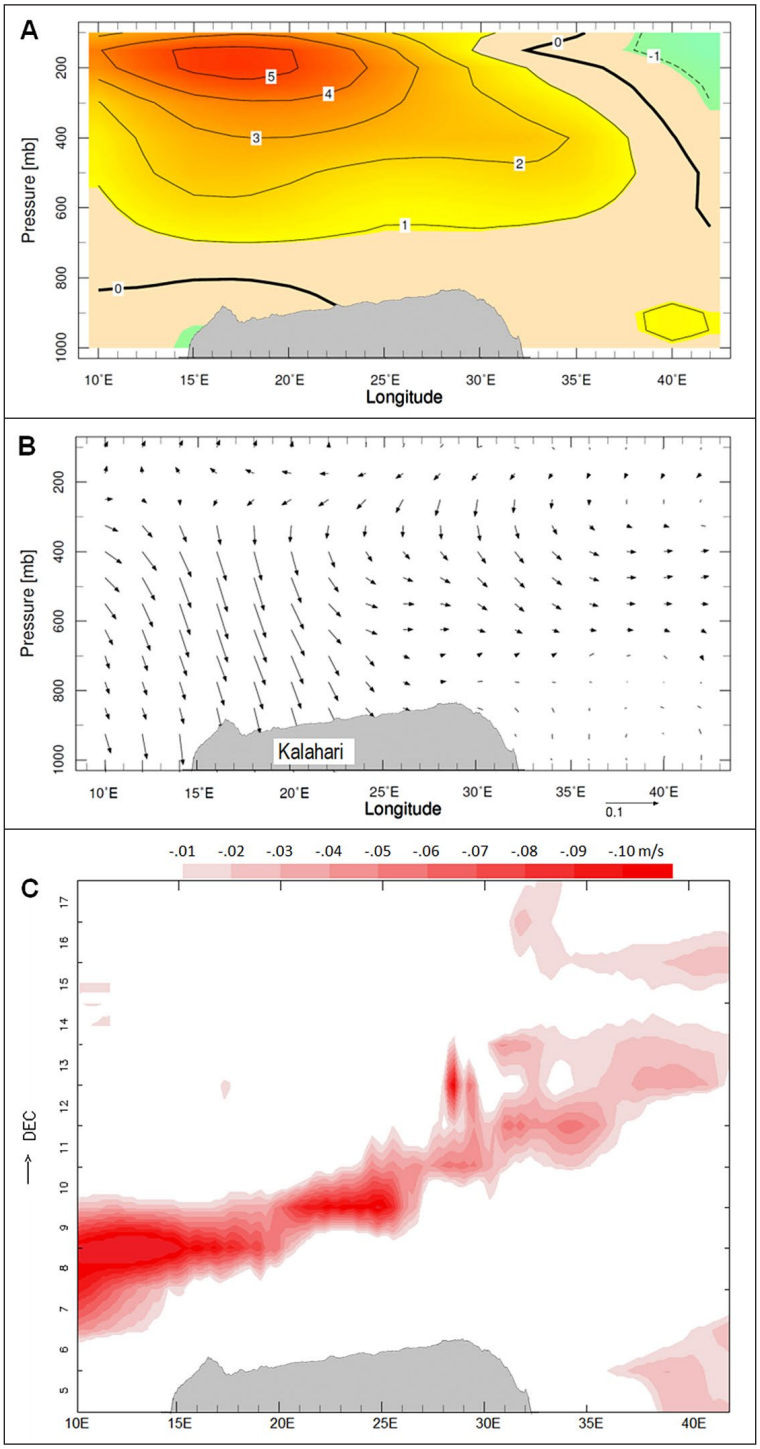

Figure 4. Vertical sections of anomalous: (a) V wind and (b) zonal circulation and subsidence, averaged 33–24°S, Oct 18–Feb 19, (c) Hovmoller plot in Dec 2018, of 500 hPa sinking motion (m/s) with topographic profile; eastward phase speed ~7 m/s. Values in (a), (b) represent departures.

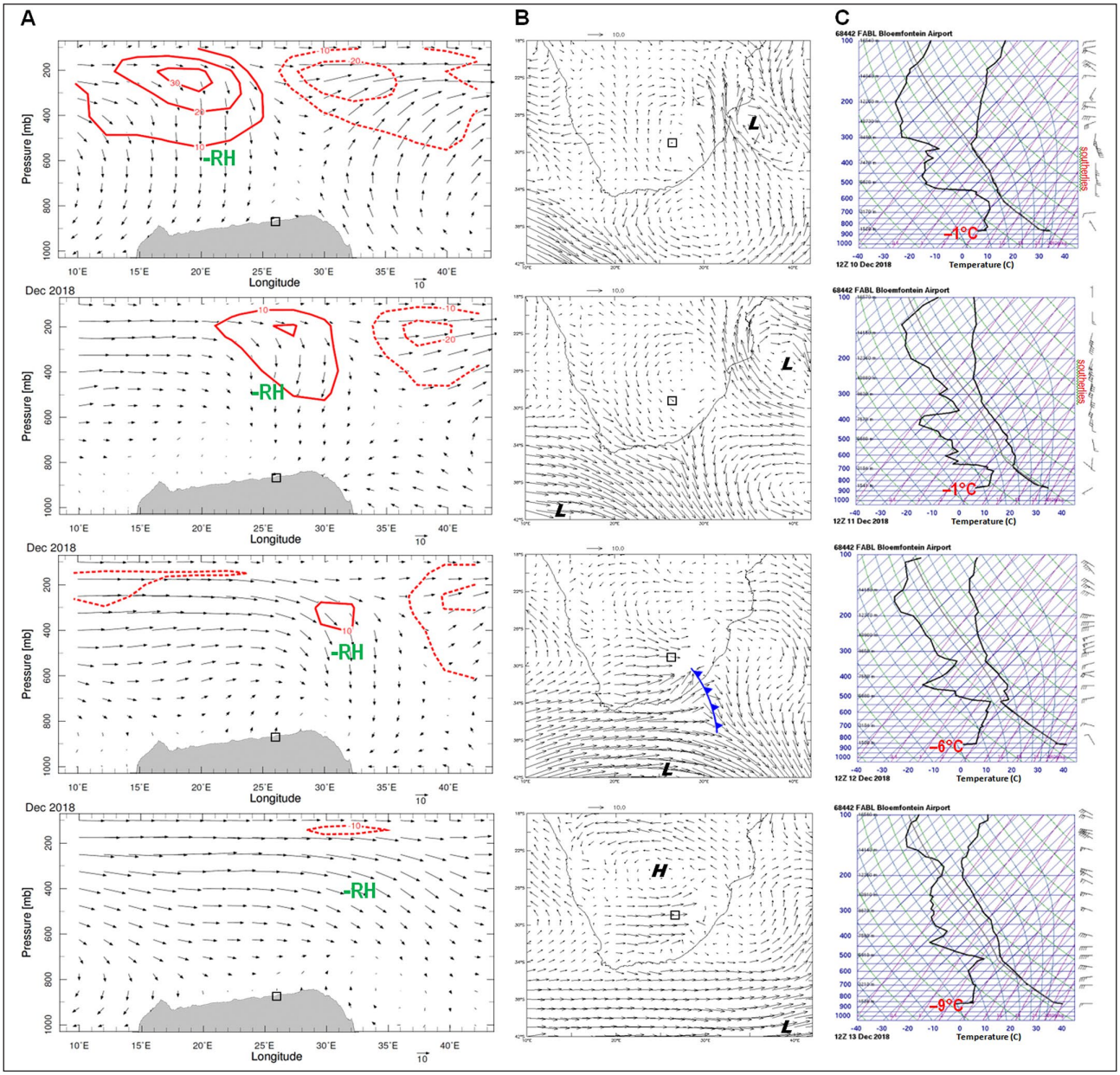

Figure 5. Meteorological sequence (top-down) 10–13 Dec 2018: (a) vertical sections average 24–33°S of zonal circulation (vector), V wind (red contour), relative humidity minimum (green), (b) maps of 850 hPa wind (vectors) with icons, (c) radiosonde profile at Bloemfontein (29°S, 26°E, denoted □), with red southerly winds (on 10–11 Dec) and surface dewpoint temperature. Values represent totals (not departures).

To track the source of dry air in this case, dust aerosols are mapped in Fig. 6a. Concentrations > 70 ppb feature prominently over the Namib Desert and spread south-eastward across the Kalahari plateau. Airflow back-trajectories arriving at Bloemfontein (29°S, 26°E) in the period 11–13 Dec 2018 (Fig. 6b) show points of origin from the cold Benguela Current and Namibian coast. The side-view reveals a conveyor of air descending from 3 000 m to 1 000 m over the 2-day period. Dry weather conditions are reflected in hourly station data at Bloemfontein from 10–14 Dec 2018 (Fig. 6c). Initially wind speeds and solar radiation varied due to the passing weather system on 10 Dec. Diurnal cycling commenced amidst declining dewpoint temperatures. Surface westerly winds reached 6 m/s by 15:00 on 13 Oct, mixing hot dusty air into the boundary layer.

Global–regional teleconnections

Global drivers of South African dry spells were analysed by point-to-field regression of the pot.evap time series (cf. Fig. 1b) in austral summer. The SST map (Fig. 7a) confirms a combined influence for the Pacific El Niño and warm-west Indian Ocean Dipole. The net OLR map (Fig. 7b) indicates that high potential evaporation over southern Africa in austral summer coincides with dry weather over eastern Brazil and the Maritime Continent. Opposing correlations (shaded blue) appear to the northeast of Madagascar and over the equatorial Pacific, indicative of deep maritime clouds. The south polar 500 hPa geopotential height correlation (Fig. 7c) demonstrates that tropical SST warming induces a ridge in the latitude band 0–20°S which tightens the pressure gradient at 30–40°S thereby accelerating the westerlies. The high-north/low-south pattern over the southeast Atlantic and trough in the Mozambique Channel promote north-eastward airflow over eSA (Fig. 7d) in dry summers. Anomalous 850 hPa westerly winds approach Cape Town (34°S), then veer north-eastward onto the plateau (30°S) and exit near Maputo (26°S). The vertical compression of airflow plays a role in equatorward veering, according to theory (Holton, 1992): $d/dt\ (\xi + f)/h$ = constant. The total derivative follows the motion; relative vorticity (ξ) and Coriolis (f) maintain balance as westerlies rise over the plateau (h). Anticyclonic curvature offsets the 1 500 m change in elevation (cf. Hartung et al., 2019), leading to equatorward winds and sinking motion that spreads dry air across eSA.

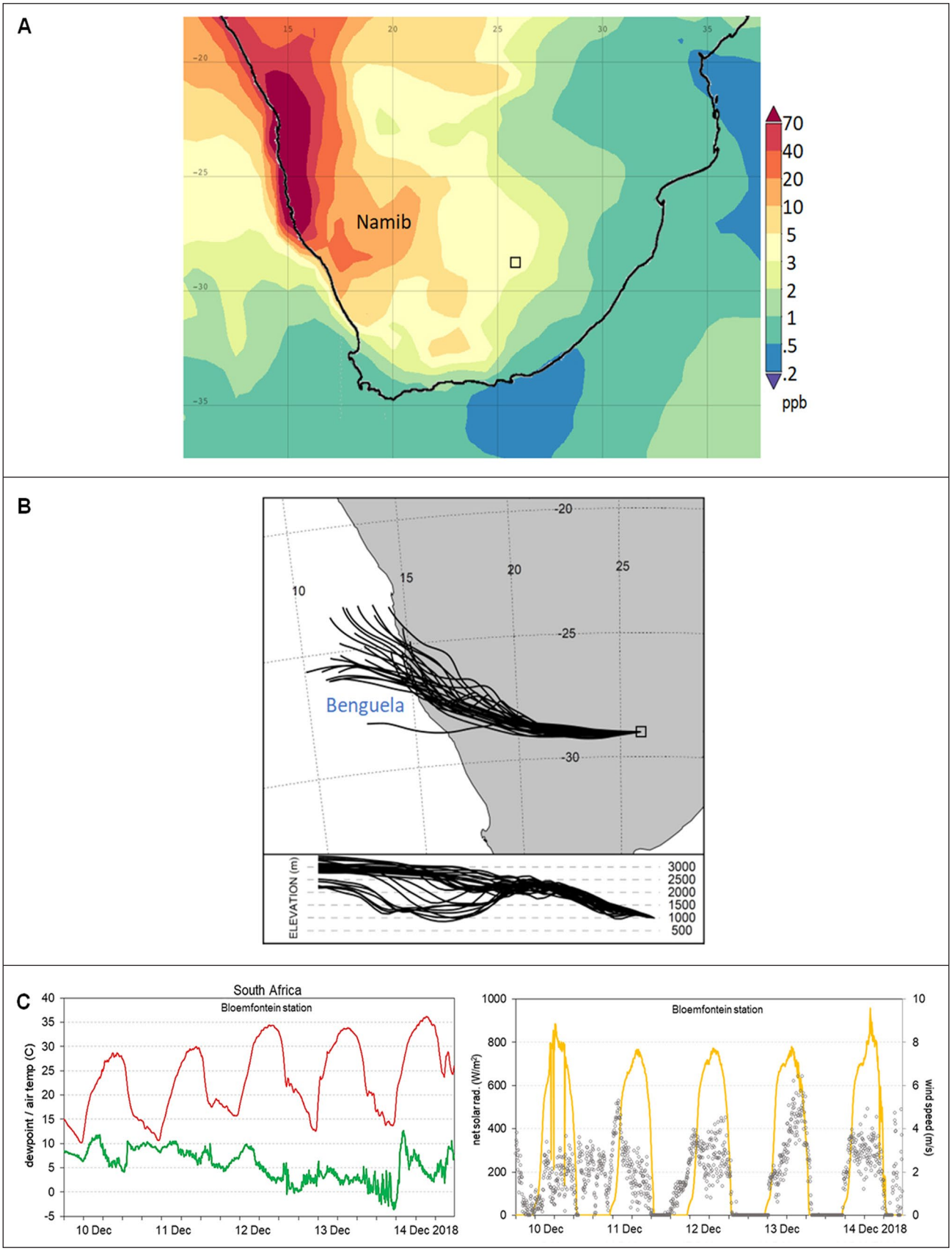

Figure 6. (a) Map of MERRA2 surface dust concentration 11–13 Dec 2018 from air chemistry assimilation and (b) back-trajectory of airflow arriving at 29°S, 26°E with side-view lower, (c) Bloemfontein □ weather station time series 10–14 Dec 2018 of dewpoint (green) and air temperature (left), solar radiation (yellow) and wind speed (grey dots). Namib Desert dust spreads across South Africa with hot dry air.

The lead–lag influence of Pacific El Niño (3.4) and Indian Ocean Dipole on Oct–Mar pot.evap over eSA is analysed in Fig. 7e and f over the period 1960–2022. Both sea temperature indices show a positive correlation (warm-phase drought) reaching +0.6. The signal is delayed for the Pacific indicating lower lead / higher lag influence, while the IOD signal is symmetrical. The temporal character reflects ocean Rossby wave coupling with the equatorial Walker Circulation in austral summer (White, 2000; Yamagata et al., 2003; Jury, 2019).

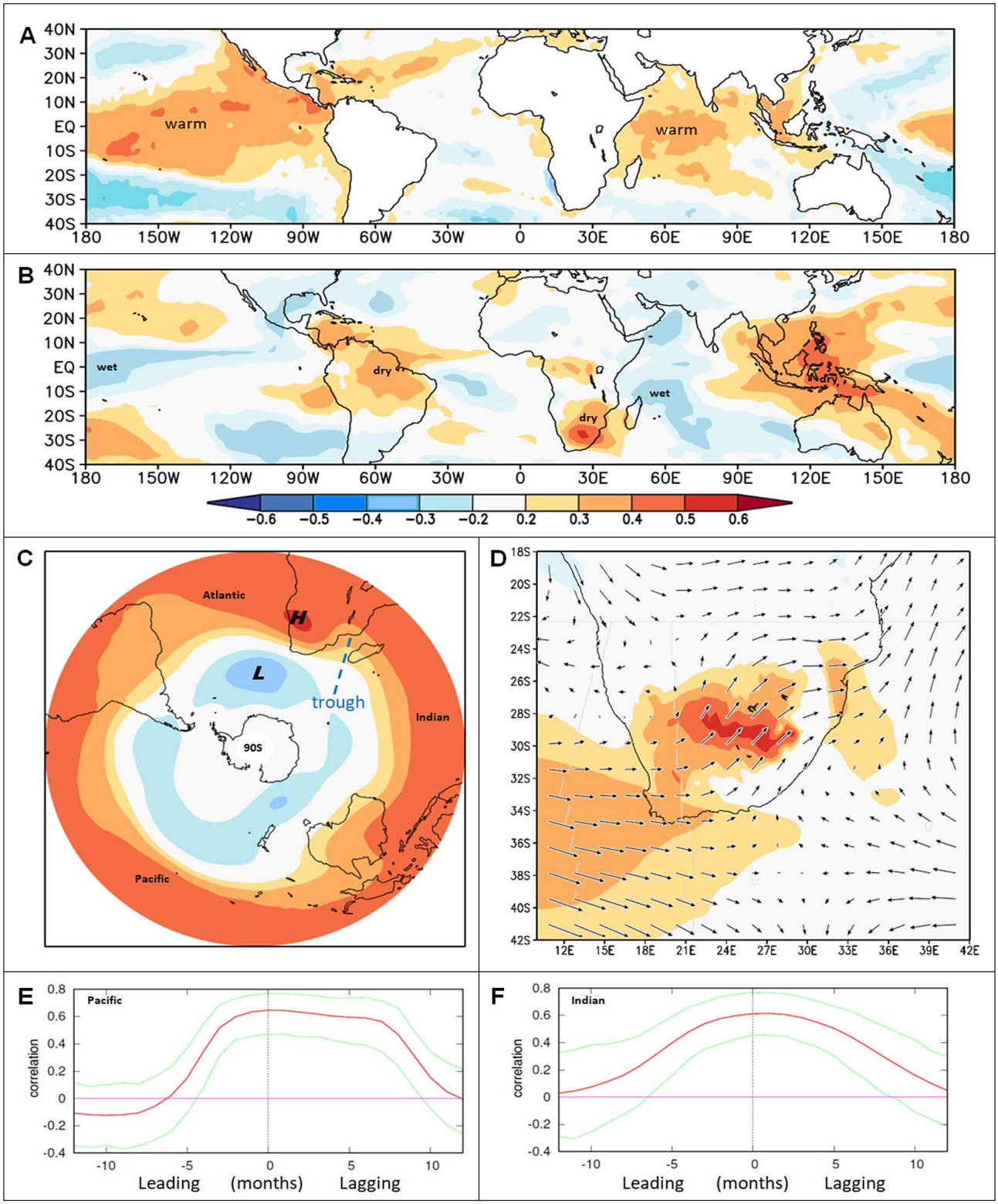

Figure 7. Correlation of eSA pot.evap time series 1960–2022 with Oct–Mar fields of: (a) global SST, (b) satellite net OLR, (c) 500 geopotential height in south polar projection with icons, and (d) local 850 hPa wind (U shaded, vectors); colour bar refers to all panels. Lag-correlation of Oct–Mar eSA pot.evap values for 1960–2022 with: (e) Pacific Nino3.4 SST and (f) IOD index, where negative refers to SST leading; $N = 63$.

Relative importance of water supply/demand

Employing runoff and river discharge to characterize water resources, the relative importance of meteorological supply (rainfall) and demand (pot.evap) is evaluated. The seasonal peak of river discharge and correlation between runoff and pot.evap are mapped in Fig. 8a. Major rivers such as the Vaal, Orange, Limpopo, and Tugela achieve discharge in excess of 200 m^3/s. Point-to-field correlation of runoff with eSA pot.evap reveals a zone of values < -0.5 with a NW axis indicating reduced frequency of cloud bands. The time series of eSA river discharge anomalies (Fig. 8b) shows wet spells in 1988, 1996, 2000, followed by diminishing water yields, consistent with Landman et al. (2001). The eSA rainfall and pot.evap lead/lag correlations are mirror images, reaching equally significant values ±0.74 with respect to river discharge from 0 to +2 months. This indicates surface water demand plays a role equal to rainfall in determining water resource availability, particularly in a globally warmed future.

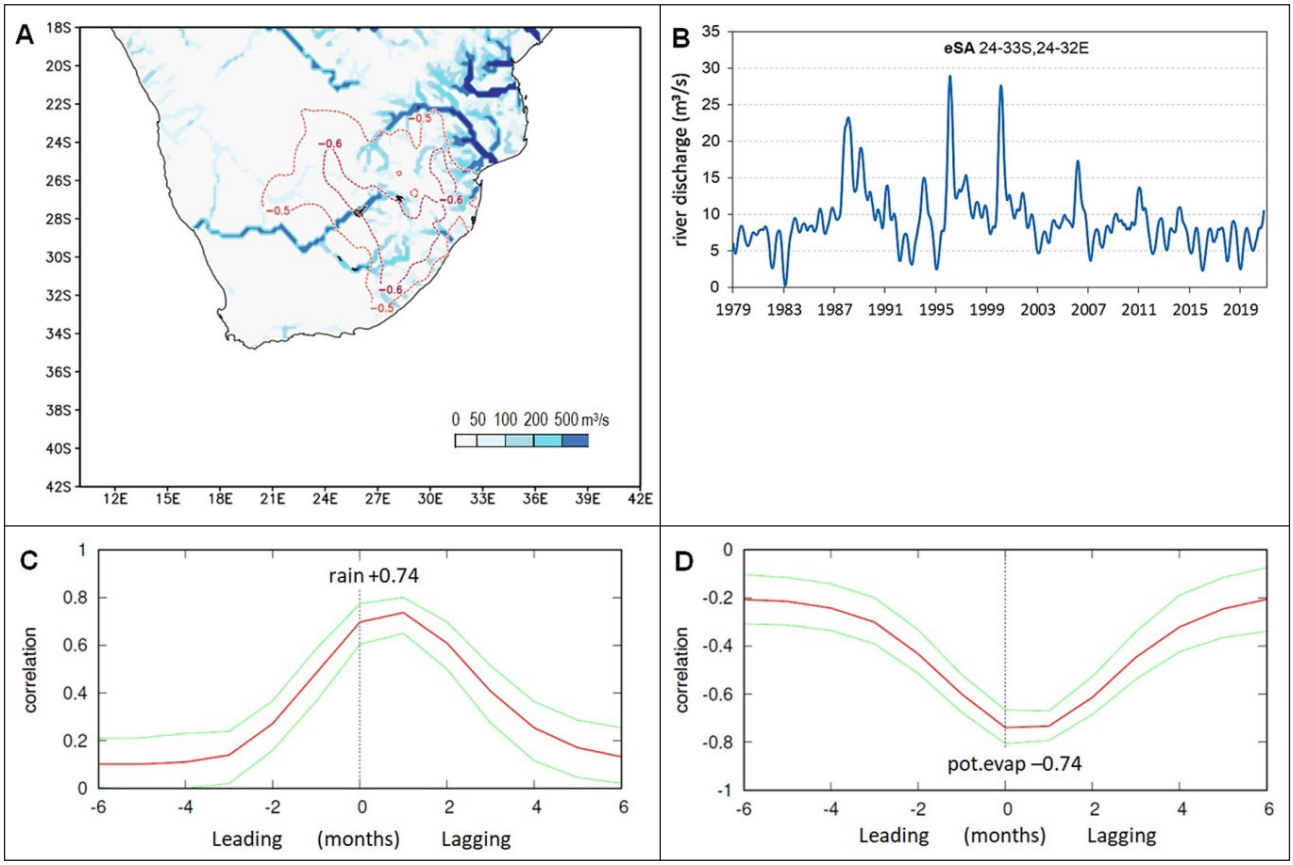

Figure 8. (a) Map of peak seasonal river discharge with dashed contours representing the correlation < −0.5 between runoff and the eSA pot. evap time series; (b) 6-month filtered time series of river discharge in the eSA area and its lag correlation with time series of: (c) CRU4 rainfall and d) ERA5 potential evaporation in the eSA area, where positive refers to discharge lagging, $N = 502$, peak values listed.

CONCLUDING DISCUSSION

Dry spells in eastern South Africa have been well studied, so what further insights have emerged? At the outset, the research considered how to characterize the rate of desiccation. No rain under cool, calm, cloudy weather produces little environmental stress compared with warm, windy, sunny weather. Surface moisture transfer to atmosphere (latent heat flux) closely follows soil moisture and vegetation fraction. The deficit variable: potential evaporation, is an alternative. It derives from sensible heat flux, and exhibits inverse responses to rainfall (cf. Fig. 8c, d) and compares favourably with (CRU4) weather station P-M and S-pan evaporation measurements (cf. Fig. 1b, 2a). ERA5 values were ~10% above eSA monthly CRU4 and ~15% below daily S-pan measurements at 30°S and 26°E, suggesting validity of this diagnostic from reanalysis.

The filtered pot.evap time series 1960–2022 averaged over eSA reflected numerous dry spells, chief among those was Oct 2018–Feb 2019. Analysing this representative season, the main source of dry air was the Namib Desert next to the cold Benguela Current. Its warm, dusty airmass spread across the Kalahari from 10–13 Dec 2018 (cf. Fig. 6a, b) behind a transient sub-tropical ridge that delivered upper-level equatorward airflow and mid-level sinking motions. Low-level westerlies spread into the Orange River Valley, bringing hot, dry, dusty air and potential evaporation ~8 mm/day. Statistical correlations confirmed the findings of earlier work (Chikoore and Jury, 2021), i.e., that eSA desiccation is underpinned by Pacific El Niño and warm-west Indian Ocean Dipole SST patterns. Dry spells were frequent and intense in the period 2015–2019, corresponding with low river discharge.

One surprising outcome was that runoff across eastern South Africa was equally correlated with rainfall and potential evaporation (±0.74), inferring that applied research on hydrological losses are just as important as gains. A further spin-off is that climate change evaluations of the water balance should use precipitation minus potential evaporation (SHF) instead of actual evaporation. Upward trends for potential evaporation against mixed outcomes for summer precipitation, suggest growing challenges for southern Africa (Caretta et al., 2022). Yet adaptive efforts to sustain crop production are 'paying off', as the South African maize yield has remained steady (Fig. A1, Appendix) despite projections of decline (Knight and Rogerson, 2019). Given the impact of pot.evap on water deficits, automatic weather stations could incorporate low-cost sonic anemometers and fast temperature sensors to measure SHF by eddy covariance ($w'T'$). Such observations would better quantify the water balance, leading to scientifically informed solutions.

ACKNOWLEDGEMENTS

S-pan data derive from the SA Hydrology Service. Satellite and reanalysis data were analysed from the KNMI Climate Explorer, IRI Climate Library, Univ Hawaii APDRC. On-going support from the South Africa Department of Higher Education and Training is appreciated.

REFERENCES

BARIMALALA R, BLAMEY RC, DESBIOLLES F and REASON CJC (2020) Variability in the Mozambique channel trough and impacts on southeast African rainfall. *J. Clim.* **33** 749–765. https://doi.org/10.1175/JCLI-D-19-0267.1

BEHRINGER DW (2007) 3.3. The global ocean data assimilation system (GODAS) at NCEP. *11th Symposium on Integrated Observing Assimilation Systems*, San Antonio TX. American Meteorological Society.

BLAMEY RC, KOLUSU SR, MAHLALELA P, et al. (2018) The role of regional circulation features in regulating El Niño climate impacts over southern Africa: A comparison of the 2015/16 drought with previous events. *Int. J. Climatol.* **38** 5668. https://doi.org/10.1002/joc.5668

CARETTA MA, MUKHERJI A, ARFANUZZAMAN M, BETTS RA, GELFAN Y, HIRABAYASHI Y, LISSNER TK, LIU J, LOPEZ GUNN E, MORGAN R and co-authors (2022) Fig 4.3d in Chapter 4. Water. In: In: Pörtner H-O, Roberts DC, Tignor M, Poloczanska ES, Mintenbeck K, Alegría A, Craig M, Langsdorf S, Löschke S, Möller V, Okem A and Rama B (eds.) *Climate Change 2022: Impacts, Adaptation and Vulnerability. Contribution of Working Group II to the Sixth Assessment Report of the Intergovernmental Panel on Climate Change*. IPCC, Cambridge University Press, Cambridge. 551–712. https://doi.org/10.1017/9781009325844.006

CHIKOORE H and JURY MR (2021) South African drought, deconstructed. *Weather Clim. Extremes* **33** 100334.

DRIVER P and REASON CJC (2017) Variability in the Botswana High and its relationships with rainfall and temperature characteristics over southern Africa. *Int. J. Climatol.* **37** 570–581. https://doi.org/10.1002/joc.5022

GHIGGI G, HUMPHREY V, SENEVIRATNE SI and GUDMUNDSSON L (2021) G-RUN ensemble: A multi-forcing observation-based global runoff reanalysis. *Water Resour. Res.* **57** e2020WR028787. https://doi.org/10.1029/2020WR028787

HARRIS I, OSBORN TJ, JONES P and LISTER D (2020) Version 4 of the CRU TS monthly high-resolution gridded multivariate climate dataset. *Sci. Data* **7** Article 109. https://doi.org/10.1038/s41597-020-0453-3

HARRIGAN S, ZSOTER E, ALFIERI L, PRUDHOMME C, SALAMON P, WETTERHALL F, BARNARD C, CLOKE H and PAPPENBERGER F (2020) GloFAS-ERA5 operational global river discharge reanalysis 1979–present. *Earth Syst. Sci. Data* **12** 2043–2060. https://doi.org/10.5194/essd-12-2043-2020

HERSBACH H, BELL B, BERRISFORD P, HIRAHARA S, HORANYI A, MUNOZ-SABATER J, NICOLAS J, PEUBEY C, RADU R, SCHEPERS D, SIMMONS A, SOCI C, ABDALLA S, ABELLAN X, BALSAMO G, BECHTOLD P, and co-authors (2020) The ERA5 global reanalysis. *Q. J. R. Meteorol. Soc.* **146** 1999–2049. https://doi.org/10.1002/qj.3803

HART NCG, WASHINGTON R and REASON CJC (2018) On the likelihood of tropical–extratropical cloud bands in the south Indian convergence zone during ENSO Events. *J. Clim.* **31** 2797–2817. https://doi.org/10.1175/JCLI-D-17-0221.1

HARTUNG K, SHEPHERD TG, HOSKINS BJ, METHVEN J and SVENSSON G (2020) Diagnosing topographic forcing in an atmospheric dataset: The case of the North American Cordillera. *Q. J. R. Meteorol. Soc.* **146** 314–326. https://doi.org/10.1002/qj.3677

HOLTON JR (1992) *An Introduction to Dynamic Meteorology*. Academic Press, New York. 511 pp.

JURY MR (2019) Global wave-2 structure of ENSO-modulated convection. *Int. J. Climatol.* **39** 5963. https://doi.org/10.1002/joc.5963

JURY MR (2022) Representing the Indian Ocean Dipole. *Phys. Oceanogr.* **29** 417–432.

KNIGHT J and ROGERSON CM (2019) *The Geography of South Africa*. Springer Nature, Switzerland, ISBN 2362-9083. 326 pp. https://doi.org/10.1007/978-3-319-94974-1

LANDMAN WA, MASON SJ, TYSON PD and TENNANT WJ (2001) Statistical downscaling of GCM simulations to streamflow. *J. Hydrol.* **252** 221–236. https://doi.org/10.1016/S0022-1694(01)00457-7

LEE HT, GRUBER A, ELLINGSON RG and LASZLO I (2007) Development of the HIRS outgoing longwave radiation climate dataset. *J. Atmos. Oceanic Technol.* **24** 2029–2047. https://doi.org/10.1175/2007JTECHA989.1

LINDESAY JA and VOGEL CH (1990) Historical evidence for Southern Oscillation-southern African rainfall relationships. *Int. J. Climatol.* **10** 679–689. https://doi.org/10.1002/joc.3370100703

LYON B (2009) Southern African summer drought and heat waves: observations and coupled model behaviour. *J. Clim.* **22** 6033–6046. https://doi.org/10.1175/2009JCLI3101.1

MALHERBE J, DIEPPOS B, MALULEKE P, STADEN M and PILLAY D (2016) South African droughts and decadal variability. *Nat. Hazards* **80** 657–681. https://doi.org/10.1175/2009JCLI3101.1

MAES WH, GENTINE P, VERHOEST NEC and MIRALLES DG (2018) Potential evaporation at eddy-covariance sites across the globe. *Hydrol. Earth Syst. Sci.* **23** 925–948. https://doi.org/10.5194/hess-23-925-2019

MASON SJ and JURY MR (1997) Climatic variability and change over southern Africa: a reflection on underlying processes. *Prog. Phys. Geogr.* **21** 23–50. https://doi.org/10.1177/030913339702100103

MAUDER M, JEGEDE O, OKOGBUE E, WIMMER F and FOKEN T (2007) Surface energy balance measurements at a tropical site in West Africa during the transition from dry to wet season. *Theor. Appl. Climatol.* **89** 171–183. https://doi.org/10.1007/s00704-006-0252-6

MCMAHON TA, PEEL MC, LOWE L, SRIKANTHAN R and MCVICAR TR (2013) Estimating actual, potential, reference crop and pan evaporation using standard meteorological data: a pragmatic synthesis. *Hydrol. Earth Syst. Sci.* **17** 1331–1363. https://doi.org/10.5194/hess-17-1331-2013

MOLOD A, TAKACS L, SUAREZ M and BACMEISTER J (2015) Development of the GEOS-5 atmospheric general circulation model: Evolution from MERRA to MERRA2. *Geosci. Model Dev.* **8** 1339–1356. https://doi.org/10.5194/gmd-8-1339-2015

PINZON JE and TUCKER CJ (2014) A non-stationary 1981–2012 AVHRR NDVI3g time series. *Remote Sens.* **6** 6929–6960. https://doi.org/10.3390/rs6086929

RAYNER NA, PARKER DE, HORTON EB, FOLLAND CK, ALEXANDER LV, ROWELL DP, KENT EC and KAPLAN A (2003) Global analyses of sea surface temperature, sea ice, and night marine air temperature since the late nineteenth century. *J. Geophys. Res.* **108** (D14) 4407. https://doi.org/10.1029/2002JD002670

SAHA S, MOORTHI S, WU X, WANG J, NADIGA S, TRIPP P, BEHRINGER D, HOU Y-T, CHUANG H-Y, IREDELL M, and coauthors (2014) The NCEP climate forecast system version 2. *J. Clim.* **27** 2185–2208. https://doi.org/10.1175/JCLI-D-12-00823.1

SAHS (South African Hydrological Service (2023) S-pan data access. URL: www.dws.gov.za/Hydrology/ (Accessed 10 February 2024).

SPERNA-WEILAND FC, TISSEUIL C, DURR HH, VRAC M and VANBEEK LPH (2012) Selecting the optimal method to calculate global reference potential evaporation from CFS Reanalysis data for application in a hydrological model study. *Hydrol. Earth Syst. Sci.* **16** 983–1000. https://doi.org/10.5194/hess-16-983-2012

STEIN AF, DRAXLER RR, ROLPH GD, STUNDER BJB, COHEN MD and NGAN F (2015) NOAA's HYSPLIT atmospheric transport and dispersion modeling system. *Bull. Am. Meteor. Soc.* **96** 2059–2077. https://doi.org/10.1175/BAMS-D-14-00110.1

VIGAUD N, RICHARD Y, ROUAULT M and FAUCHEREAU N (2009) Moisture transport between the south Atlantic Ocean and southern Africa: relationships with summer rainfall and associated dynamics. *Clim. Dyn.* **32** 113–123. https://doi.org/10.1007/s00382-008-0377-7

WHITE WB (2000) Coupled Rossby waves in the Indian Ocean on interannual time scales. *J. Phys. Oceanogr.* **30** 2972–2989. https://doi.org/10.1175/1520-0485(2001)031<2972:CRWITI>2.0.CO;2

YAMAGATA T, BEHERA SK, LUO J-J, MASSON S, JURY MR and RAO SA (2003) Coupled ocean-atmosphere variability in the tropical Indian Ocean. In: Wang C, Xie S-P and Carton JA (eds) *Earth Climate: Ocean-Atmosphere Interaction*. Monograph 147. American Geophysical Union. 189–212. https://doi.org/10.1029/147GM12

APPENDIX

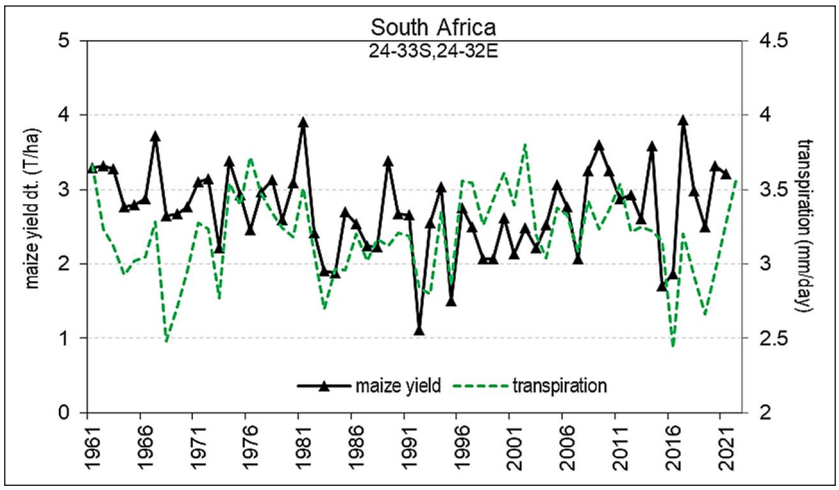

Figure A1. Time series of (detrended) South African annual maize yield and eSA transpiration during the preceding summer, based on ERA5 latent heat flux and satellite vegetation colour fraction